Effect of Fluid Properties on Contact Angles in the Eagle Ford Shale Measured with Spontaneous Imbibition

Joanna McFarlane,* Victoria H. DiStefano, Philip R. Bingham, Hassina Z. Bilheux, Michael C. Cheshire, Richard E. Hale, Daniel S. Hussey, David L. Jacobson, Lindsay Kolbus, Jacob M. LaManna, Edmund Perfect, Mark Rivers, Louis J. Santodonato, and Lawrence M. Anovitz

ACCESS | Metrics & More | Article Recommendations

ABSTRACT: Models of fluid flow are used to improve the efficiency of oil and gas extraction and to estimate the storage and leakage of carbon dioxide in geologic reservoirs. Therefore, a quantitative understanding of key parameters of rock−fluid interactions, such as contact angles, wetting, and the rate of spontaneous imbibition, is necessary if these models are to predict reservoir behavior accurately. In this study, aqueous fluid imbibition rates were measured in fractures in samples of the Eagle Ford Shale using neutron imaging. Several liquids, including pure water and aqueous solutions containing sodium bicarbonate and sodium chloride, were used to determine the impact of solution chemistry on uptake rates. Uptake rate analysis provided dynamic contact angles for the Eagle Ford Shale that ranged from 51 to 90° using the Schwiebert−Leong equation, suggesting moderately hydrophilic mineralogy. When corrected for hydrostatic pressure, the average contact angle was calculated as $76 \pm 7°$, with higher values at the fracture inlet. Differences in imbibition arising from differing fracture widths, physical liquid properties, and wetting front height were investigated. For example, bicarbonate-contacted samples had average contact angles that varied between $62 \pm 10°$ and $\sim 84 \pm 6°$ as the fluid rose in the column, likely reflecting a convergence−divergence structure within the fracture. Secondary imbibitions into the same samples showed a much more rapid uptake for water and sodium chloride solutions that suggested alteration of the clay in contact with the solution producing a water-wet environment. The same effect was not observed for sodium bicarbonate, which suggested that the bicarbonate ion prevented shale hydration. This study demonstrates how the imbibition rate measured by neutron imaging can be used to determine contact angles for solutions in contact with shale or other materials and that wetting properties can vary on a relatively fine scale during imbibition, requiring detailed descriptions of wetting for accurate reservoir modeling.
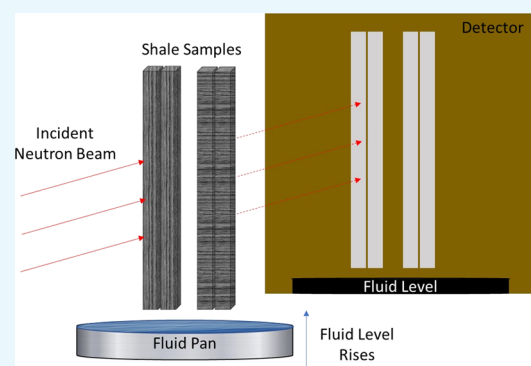
INTRODUCTION

Shale formations are increasingly important for oil and gas recovery and as potential seals for geologic carbon sequestration.[1] However, fracture propagation and flow modeling in these reservoirs are needed to improve recovery efficiency and sequestration reliability. Although real-time data collection can be used to map fractures, many hydraulic fracture propagation models used to predict fracture networks and model fluid flow through those networks are based on conventional sandstone reservoirs, which are distinctly different from shales.[2] This is partly because fluid flow through shale reservoirs is governed by complex fluid−mineral interactions, as well as differences in mechanical and surface properties.[3] These become increasingly complex and important for modeling and recovery efforts when multiple phases (e.g., oil, water, brine, air, carbon dioxide) are present in the reservoir and in the rock (calcite, quartz, clay, etc.).[4] One important fluid−mineral interaction is wettability,[5−8] which describes the preference of the solid rock to be in

contact with one fluid, such as water, rather than another, such as air.[9] Wettability can be measured in terms of the contact angle tangential to the interface between a drop of one fluid (e.g., water) and a solid surface exposed to a second fluid (e.g., air), with the angle drawn through the aqueous phase. The contact angle of a rock−liquid−air interface, θ, is defined by the equilibrium of three interfacial forces according to Young's equation[10]

$$\cos \theta = \frac{\gamma_{AR} - \gamma_{RF}}{\gamma_{FA}} \tag{1}$$

where γ_{AR}, γ_{RF}, and, γ_{FA} are the interfacial tensions of air–rock, rock–liquid, and liquid–air boundaries, respectively. Similarly, wetting fluid uptake can be described in a dynamic environment by advancing contact angles formed at the forward edge of liquid expansion when liquid flows through a fracture.

In this study, contact angles formed during spontaneous imbibition were determined for fractures in Eagle Ford Shale formation (Texas) samples using real-time neutron radiographic imaging. Spontaneous imbibition occurs when a wetting fluid penetrates voids in a rock, displacing a nonwetting liquid or gas, due to attractive forces between fluid molecules.[11] Because the imbibition rate is a function of the interaction between the fluids involved and the rock, it can be used to estimate fluid/rock dynamic contact angles and thus provides a method for quantifying the aforementioned relative interfacial tensions.[3] Contact angles are influenced by rock properties, such as mineralogy and fracture roughness, and fluid properties such as viscosity.[12–14] Thus, if the data are to be useful for improving subsurface models and resource extraction, contact angles must be measured between relevant fluids and rock surfaces.

To assess the effect of fluid chemistry on imbibition rates and contact angles in shales, the height of the imbibing wetting front was measured as a function of time into a polished, rectangular fracture between blocks of Eagle Ford Shale using neutron imaging (i.e., radiography and tomography). Three solutions were imbibed: water, water saturated with sodium bicarbonate at room temperature, 21 °C, and water containing sodium chloride at a concentration of 0.6 mol·L^{-1}. These were chosen because chloride brines and carbonate-bearing fluids are commonly present in subsurface aqueous systems, including those important to carbon capture and sequestration.[15,16] The saturated sodium bicarbonate solution simulates subsurface conditions in geological carbon sequestration reservoirs, and the sodium chloride solution represents saline brines present in a wide variety of geological environments, including many oil and gas reservoirs and seawater.[17] The imbibition rates of these two solutions were compared with that of deionized (DI) water in samples of the same rock, as reported previously,[3] which served as a control.

Experimental Design. Neutron imaging provides a highly accurate, high-contrast method for quantitatively determining the spontaneous imbibition rate of hydrogen-rich fluids, such as water or oil, into fractured or porous media in real time. This is because the large neutron-scattering cross section of hydrogen provides a high contrast with surrounding rock materials.[3,18–22] In neutron imaging, the intensity of a beam passing through a sample is detected using a scintillator or microchannel plate. Neutron transmission can be modeled using the Lambert–Beer law[23]

$$T = \frac{I}{I_0} = e^{-N\sigma_c t_s}$$ (2)

where I is the measured intensity, I_0 is the incident intensity, T is the transmission, N is the atom density, σ_c is the total neutron cross section (a property of the atoms present), and t_s is the thickness of the sample. The transmission intensity is collected on a 2D detector as serial radiographs to show the evolution of the system with time. Images can also be taken before and after the experiment while rotating the sample to allow for 3D tomographic reconstruction. This process is to be used to collect tomographic images of the fluid uptake in

progress. Although neutrons can activate the sample, such activation that does occur in typical silicate rocks is relatively short lived. Neutron imaging is, otherwise, nondestructive and can currently achieve resolution down to 15–20 μm[24] and, in rare cases, even less.[25,26] This is coarser than obtainable with X-ray techniques but sufficient for the fractures in, and goals of, this study. Additionally, although fluxes available at neutron sources are relatively low compared with those available at synchrotron X-ray sources, this is mitigated by the high contrast of hydrogen-bearing fluids in neutron imaging. Neutron imaging can, therefore, produce as many as 100 images a second and thus is ideal for the real-time imaging of dynamic fluid flow in fractured and porous media.[3,18,19,27]

Predicting Spontaneous Imbibition: Models for Capillary Rise. Spontaneous imbibition is a capillary rise phenomenon in which interfacial attractive forces between fluid molecules cause fluids to rise in tubes, fractures, or pore structures with small-pore diameters. This has been used to describe the flow of water through shales.[28] Several fundamental equations have been developed that describe the forces that govern fluid rise in cylindrical capillaries. These were reviewed in detail by Peng.[29] Such equations are vital for constructing and understanding models of spontaneous imbibition. The modified Young–Laplace equation, shown in eq 3, expresses the capillary pressure, P_c, or the pressure difference across an interface that separates two immiscible fluids as

$$P_c = \frac{2\sigma \cos \theta}{r}$$ (3)

where r is the radius of the meniscus, σ is the surface tension at the fluid–air interface, and θ is the contact angle between the two fluids.[30] The dynamics of capillary uptake can be described using the Hagen–Poiseuille equation, which describes the laminar flow of an incompressible Newtonian fluid in a capillary as

$$Q = \frac{\pi r^4 \Delta P}{8\eta h}$$ (4)

where Q is the flow rate, h is the height of the wetting front, η is the viscosity, and ΔP is the change in pressure across the air–water interface. The flow rate is equal to the rate of change in the height of the wetting front, dh/dt, multiplied by the cross-sectional area of the flow, A. In capillary flow, three pressures are acting on the system: atmospheric pressure P_a, hydrostatic pressure P_h, and capillary pressure P_c. Assuming a circular flow cross section in eq 4, the Hagen–Poiseuille equation can be rewritten to show the rate of capillary rise as

$$\frac{dh}{dt} = \frac{r^2(P_a + P_h + P_c)}{8\eta h}$$ (5)

If the capillary has two open ends as it does in the experiments described here, then $P_a = 0$. Combining the Young–Laplace equation (eq 3) for capillary pressure with the Hagen–Poiseuille equation (eq 5) for the flow rate in a capillary tube—and assuming that both ends of the tube are exposed to the same atmospheric pressure—yields the flow equation in terms of the capillary and fluid properties (Washburn 1921)[31]

$$\frac{dh}{dt} = \frac{r^2}{8\eta h}\left(\frac{2\sigma \cos \theta}{r} - h\rho g\right)$$ (6)

This model does not account for the effects of inertia, which depend on the fluid viscosity and constrain the initial uptake rate.[13]

If the effect of hydrostatic pressure, $h\rho g$, is ignored, integrating eq 6 generates the Washburn−Lucas equation[31,32]

$$h = \sqrt{\left(\frac{\sigma r \cos \theta}{2\eta}\right)t} \tag{7}$$

Equation 7 indicates that the height of the fluid column increases as a linear function of the square root of time with a slope referred to as the sorptivity.[18,20,21] This equation has been used to describe spontaneous imbibition in cylindrical capillaries over short time scales.[18,33] Other models have been proposed for channels of various geometries using approaches similar to that of Washburn and Lucas.[18,34−37] These also predict a linear dependence of the wetting front height on the square root of time. For instance, Schwiebert and Leong provided a simple model for imbibition between parallel plates.[35] This assumes that the width, w, of the channel is orders of magnitude smaller than its length, l, and describes the height of the column as

$$h = \sqrt{\left(\frac{w\sigma \cos \theta}{3\eta}\right)t} \tag{8}$$

This equation differs only slightly from the Washburn−Lucas equation and is simply altered for imbibition in a rectangular capillary with an elliptical meniscus.

In this work, the Schwiebert and Leong model[35] (eq 8) was compared with imbibition data to determine contact angles in the Eagle Ford Shale. The geometry on which this model is based should be appropriate for the experimental design. However, it only describes early-time uptake through fractures with unreactive, completely flat surfaces. Thus, an additional analysis was performed using a transient approach developed by Cai and colleagues that includes the $h\rho g$ term.[38] Their expression is generalized for a capillary of any size or shape with diameter λ as

$$\frac{dh}{dt} = \frac{\lambda\sigma \cos \theta}{8\eta\tau^2}\left(\frac{1}{h}\right) - \frac{\lambda^2 \rho g}{32\eta\tau^2} \tag{9}$$

Cai's model also introduced tortuosity, τ, which is the ratio of the rate of rising in a cylindrical capillary to that in a vertically straight capillary. Besides tortuosity, the analysis includes other adjustable parameters, including: fluid properties, channel width, and wettability expressed as $\cos \theta$. The model can be expressed as the slope and intercept for the rate of change of height with reciprocal height. Combining this equation with X-ray computed tomography data to characterize the channel width in our experimental samples enabled us to optimize the fit to derive the contact angle.

Both the Schwiebert−Leong and the Cai models were evaluated in this study to examine the applicability of various simple imbibition models for describing shale−fluid interactions in which surface roughness and mineralogy are important.

Experimental Approach. Shale samples were obtained from an outcrop of the Eagle Ford Shale formation purchased from Kocurek Industries. Six samples of synthetic fractures created from paired shale blocks were prepared for analysis. Each block was 12.7 mm × 12.7 mm × 152.4 mm. Three of the synthetic fractures were oriented perpendicular to the shale

bedding, and three were oriented parallel to the bedding. Before imbibition, the shale mineralogy was measured with X-ray diffraction and quantified via Rietveld refinement.[39] Table 1 shows the main mineral components from the sample analysis and the reported range of compositions of the Eagle Ford Shale.[40]

Table 1. Mineral Compositions of Eagle Ford Shale Formation Determined from X-ray Diffraction

	quartz (%)	calcite (%)	smectite (%)	kaolinite (%)	pyrite (%)	other (%)
Eagle Ford (current study)	22	63	14	1	<1	10
Cermake and Schrieber (2014)	22	63	25—clay			

Two sample sets were prepared for imbibition experiments for each of the dissolved salts: sodium bicarbonate and sodium chloride. Each set contained one sample with the synthetic fracture oriented parallel to bedding and one with the fracture oriented perpendicular to bedding. The sample fracture widths were characterized using X-ray computed tomography (CT) scans performed at Argonne National Laboratory's Advanced Photon Source using the GSECARS tomography beamline (13-BM-D). The CT scans were converted into a color-coded 3D plot corresponding to the scaler values of the fracture thickness (Figures 1−3). CT scans were taken at the following distances along the sample, as measured from the surface initially in contact with the imbibing fluid: 0−3, 18−21, and 50−53 mm.

EF 25 Fracture: Bottom 3 mm - Thickness (Micrometers)

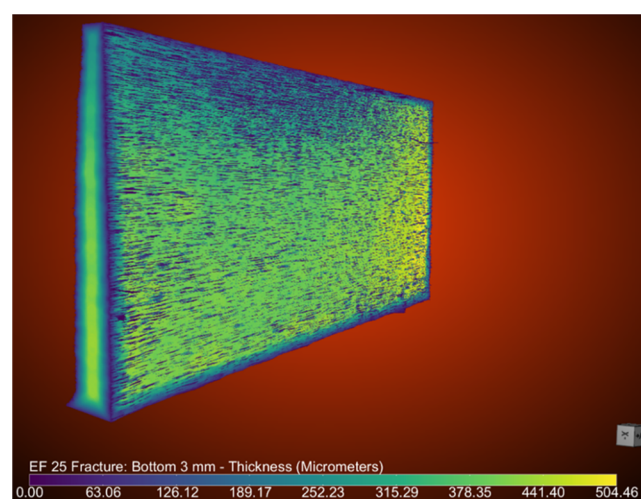| 0.00 | 63.06 | 126.12 | 189.17 | 252.23 | 315.29 | 378.35 | 441.40 | 504.46 |

Figure 1. Bottom 3 mm of the EF-HCO3-PR fracture. The wedge is the fracture, with the height being 3 mm and the breadth being 12.7 mm. The color indicates the thickness of the fracture according to the color bar. This area had the largest median fracture width (∼398 μm) observed of all of the samples.

$NaCl$ and $NaHCO_3$ brines were prepared as contact fluids. Eagle Ford formation salinity varies from 35 to 100 g·L^{-1} and is mainly NaCl.[41] The NaCl solution prepared for imbibition, 36 g·L^{-1}, is at the low end of this range. The calcium content of the Eagle Ford has been reported by the USGS as being highly variable, from 0.5 up to the 8 g·L^{-1}, or 0.01 to 0.2 mol·L^{-1}.[42] In our system, the bicarbonate had a concentration of
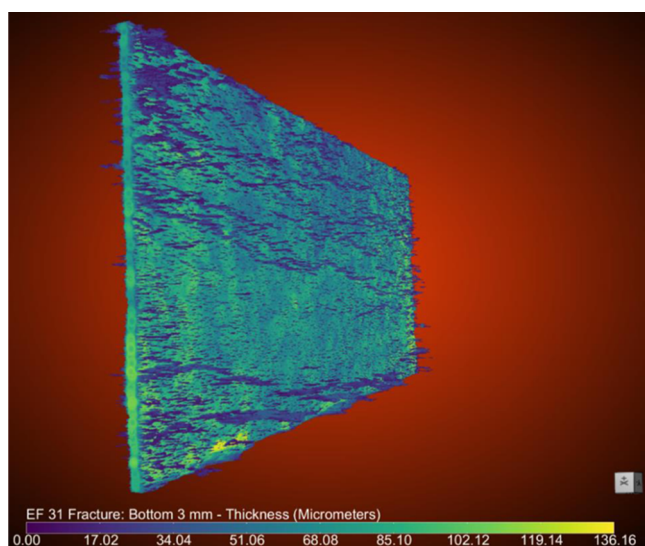
Figure 2. Bottom 3 mm of the EF-NaCl-PR fracture. The wedge is the fracture, with the height being 3 mm and the breadth being 12.7 mm. The color indicates the thickness of the fracture according to the color bar. This fracture shows additional structure obvious in some samples.
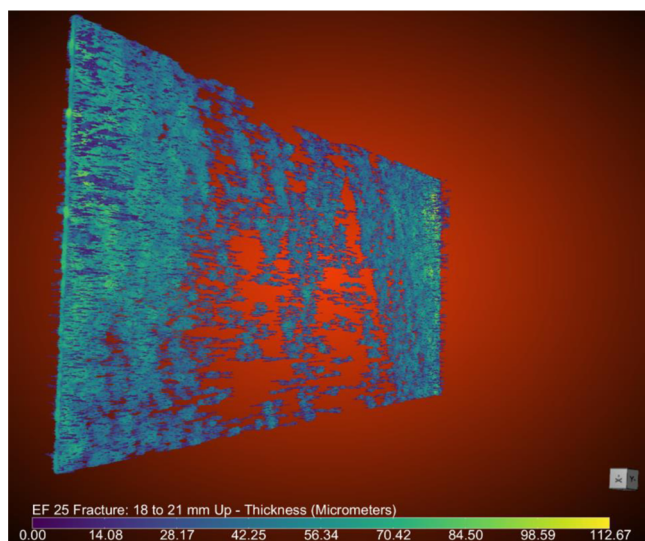

Figure 3. EF-HCO3-PR fracture 18−21 mm from the surface of the fracture in contact with the imbibition fluid. The wedge is the fracture, with the height being 3 mm and the breadth being 12.7 mm. The color indicates the thickness of the fracture according to the color bar. This fracture appears to be disjoint because parts were indistinguishable from the matrix or had widths below 3.68 μm, which was the resolution of the measurement.

0.54 mol·L^{-1}, or more than double that expected in produced water. However, in this study, we were also exploring the injection of bicarbonate brines for CO_2 sequestration and thus were interested in the behavior of higher concentration fluids.

Spontaneous imbibition was measured for all samples at the BT-2 neutron imaging facility at the National Institute of Standards and Technology Center for Neutron Research. As in previous studies, the fractured samples were oriented with the neutron beam directed through the plane of the fracture oriented vertically, as illustrated in Figure 4.[3,43] The fluid was slowly raised into contact with the fractured samples, at which point the imbibition experiment was initiated. After the initial
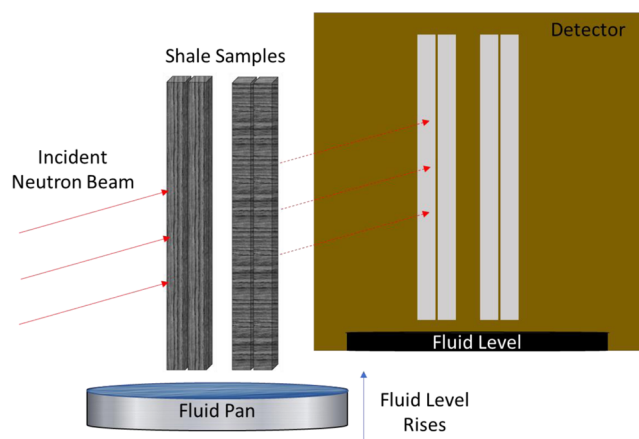

Figure 4. Schematic of neutron-imaging imbibition experiments. Only one sample was analyzed at a time, but the sample depiction shows a sample with the fracture oriented parallel to the bedding (left) and perpendicular to the bedding (right).

imbibition experiments, the samples were soaked in DI water and dried at 105 °C. Imbibition was then repeated on all samples, except for EF-HCO3-PL, in which the fluid did not imbibe into the fracture because the drying cycle had not reached completion. A control sample set with DI water as the imbibing fluid, EF-DI-PR and EF-DI-PL, was analyzed in a previous study.[3] The results are included here for comparison.

Table 2 lists the sample names, abbreviations, fracture orientations, and the imbibition fluid for each experiment. The properties of the fluids are given in Table 3.[44−48]

Table 2. Sample Matrix of the Spontaneous Imbibition Experiments

sample name	abbreviation	fracture orientation to bedding	fluid
Eagle Ford DI-1	EF-DI-PR	perpendicular	water
Eagle Ford DI-2	EF-DI-PL	parallel	water
Eagle Ford HCO3-1	EF-HCO3-PR	perpendicular	sodium bicarbonate
Eagle Ford HCO3-2	EF-HCO3-PL	parallel	sodium bicarbonate
Eagle Ford NaCl-1	EF-NaCl-PR	perpendicular	sodium chloride
Eagle Ford NaCl-2	EF-NaCl-PL	parallel	sodium chloride

■ RESULTS

Fracture Width. The thickness values measured for each fracture by X-ray CT were combined into a histogram with 4 μm bins (Figure 5). The fracture thicknesses for each sample showed more than one peak and so were fit to multipart Gaussian distributions presented in Table 4 as measured from the end of the sample initially in contact with the fluid. Medians for the overall distribution are reported in Table 4, along with the results for constituent peaks: location, full width at half-maximum (FWHM), and area. Most fracture widths could be represented by two distributions: one common to all samples at 15−20 μm probably reflecting the size of the grit used for sample polishing and one broader distribution representative of the fracture width. Hence, the median did not include the artifact widths below 20 μm. Some samples showed additional complexity at the entrance, notably EF-

Table 3. Fluid Properties

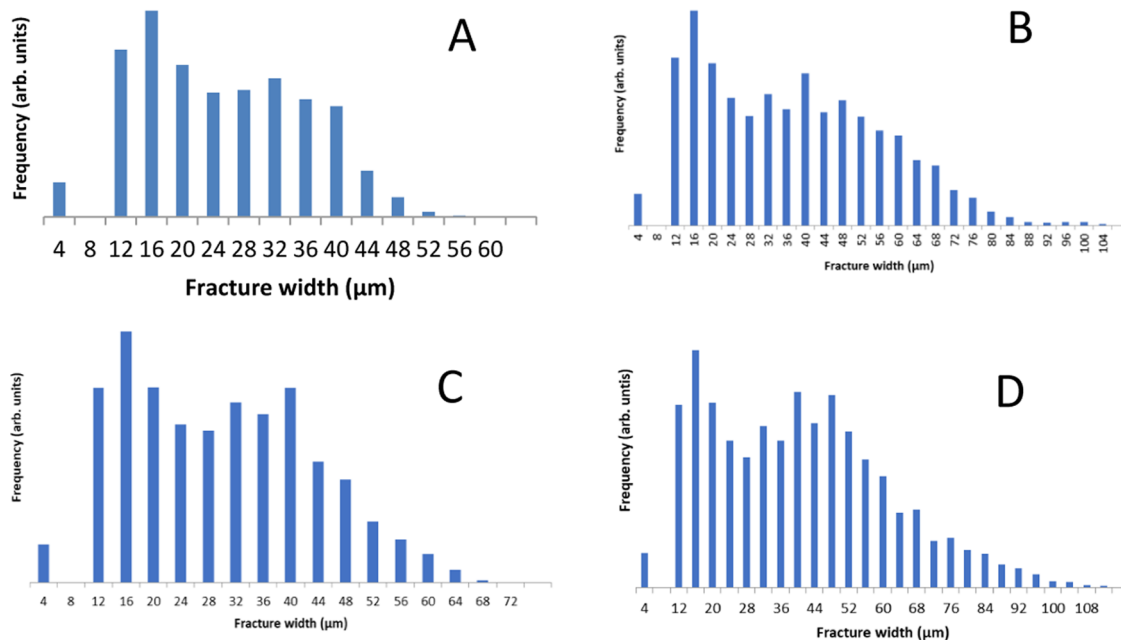| solution	concentration (mol·L^{-1})	viscosity, η (mPa·s)	surface tension, σ (mN·m^{-1})	density (g·cm^{-3})	references
sodium bicarbonate	1.1	1.27	73	1.1	44–46
sodium chloride	0.6	1.06	74	1.2	46–48
water		1.00	72	1.0	46

Figure 5. Histograms of fracture widths measured in 3 mm long slices centered at 50 mm from the contacting surface for the following samples: (A) EF-HCO3-PR, (B) EF-HCO3-PL, (C) EF-NaCl-PR, and (D) EF-NaCl-PL, respectively.

HCO3-PR and EF-HCO3-PL. All of the fractures were wider at the bottom, the end that contacted the imbibing fluid, and progressively narrowed further up the fracture with EF-HCO3-PR being the most dramatic case.

At 50−53 mm from the "contacting" bottom surface of the fracture, regions within the fractures appeared to become isolated in our images because the connections were smaller than the 3.68 μm voxel edge length. This is particularly notable for sample EF-HCO3-PR (Figure 3). This could imply that the fractures were closed in these areas, but it is more likely that they were so narrow as to be indistinguishable from the matrix at the resolution of the image. As imbibition was observed in all samples, the latter is likely the correct interpretation; however, the narrowing affected fluid uptake, as discussed below.

Fluid Imbibition into Fractures. The height of the wetting front with respect to time was quantitatively calculated from neutron images following the procedure described by DiStefano and colleagues.[3] This method fits an error function along the imbibition path for each time-resolved image with the center of the error function plus or minus one standard deviation being defined as corresponding to the fluid height. Figure 6 shows the height of the wetting front with respect to time for all six experiments, including those reported earlier for pure water (EF-DI-PR and EF-DI-PL) for comparison.[3] The increased uncertainty in the wetting height with time arises from two sources. First, the noise in the images increases, which causes uncertainties in the algorithm used to determine the height. Second, a general widening of the uptake front with time may have arisen from fluid penetration into the shale matrix.[3] The maximum hydrostatic pressure calculated for the

samples ranged from 150 to 180 Pa depending on the final height of the fluid. Although some fractures were fully wetted along the entire fracture, others appeared to reach an equilibrium height (i.e., the height at which the capillary pressure is balanced by the hydrostatic pressure).

Equation 8 was used to model the rate of imbibition into the fracture and determine the contact angle. The sorptivity, S, was determined as the slope of the height of the wetting front as a function of the square root of time, $t^{0.5}$, for each sample. However, a single square root of time dependence did not adequately describe the data from these samples, which showed more than one linear region in the uptake plots. Regressed slopes are presented in Figure 6 and Table 5 divided into a series of numbered time intervals for each of the six samples. The first region, which went from 0 s to as much as 3.2 s, showed a relatively slow imbibition rate for all samples (2−9 mm·s$^{-0.5}$), likely affected by inertial drag at the fracture entrance.[49] The second region, corresponding to several seconds, was much faster with sorption rates from 15 to 25 mm·s$^{-0.5}$. In region 3, continuing to nearly 40 s, the sorption rate slowed almost to the initial rate (5−17 mm·s$^{-0.5}$). The pattern became noisier after that point, with effects arising from the specific geometries of the samples and fractures. In one sample, EF-NaCl-PR, imbibition was complete in three stages, whereas for EF-DI-PR, four stages were required. The other samples did not achieve complete wetting during the observation time but showed additional variations in flow rate; EF-DI-PL and EF-NaCl-PL had four stages, and EF-HCO3-PL had five stages, indicated as markings on the photograph shown in Figure 7. The data for EF-HCO3-PR are incomplete due to the premature termination of the experiment. However,

Table 4. Fracture Widths of Samples Determined with X-ray CT

sample ID	median (μm)	peak position (μm)	relative height[b]	FWHM (μm)	relative area[c]
EF-DI-PR[a] 0−153 mm	28	35	1.00	17	1.00
EF-DI-PL[a] 0−3 mm	48	49	1.00	20	1.00
EF-DI-PL[a] 75−78 mm	70	56	0.55	24	0.38
		92	0.45	48	0.62
EF-DI-PL[a] 149−152 mm	64	68	1.00	49	1.00
EF-HCO3-PR 0−3 mm	191	28	0.26	22	0.09
		104	0.22	116	0.40
		253	0.45	60	0.42
		368	0.07	80	0.09
EF-HCO3-PR 18−21 mm	40	15	0.38	11	0.17
		40	0.62	35	0.83
EF-HCO3-PR 50−53 mm	31	16	0.58	15	0.57
		34	0.42	15	0.43
EF-HCO3-PL 0−3 mm	73	19	0.13	24	0.12
		69	0.59	26	0.63
		97	0.28	22	0.25
EF-HCO3-PL 18−21 mm	52	16	0.33	16	0.22
		55	0.67	28	0.78
EF-HCO3-PL 50−53 mm	42	15	0.54	12	0.24
		41	0.46	44	0.76
EF-NaCl-PR 0−3 mm	58	19	0.37	20	0.26
		62	0.63	34	0.74
EF-NaCl-PR 50−53 mm	35	15	0.53	13	0.37
		36	0.47	27	0.63
EF-NaCl-PL 0−3 mm	86	15	0.27	17	0.19
		39	0.12	21	0.10
		90	0.61	30	0.71
EF-NaCl-PL 18−21 mm	54	17	0.31	14	0.19
		57	0.69	27	0.81
EF-NaCl-PL 50−53 mm	44	15	0.46	12	0.20
		45	0.54	40	0.80

[a]Average fracture width in samples EF-DI-PR and EF-DI-PL were evaluated at different fracture heights (DiStefano et al. 2017). [b]Height of each peak maximum as a fraction of the sum of the peak heights for each scan. [c]Area of each peak as a fraction of the sum of the peak areas for each scan.

for all of these samples, the rapid imbibition in the second stage was followed by a period of slower imbibition.

Because of the apparent complexity of the imbibition, the data were fit using a function that includes the effect of hydrostatic pressure,[18] with fracture widths, λ, determined by X-ray CT scans. The approach was to first determine the slope of eq 9, $\frac{\lambda\sigma\cos\theta}{8\eta\tau^2}$, to provide an initial value for $\cos\theta$. As a simple linear fracture was being modeled, the tortuosity was set to 1. The properties of the fluid and the imbibition height were then used to calculate the time as a function of height. Contact angles determined from optimized fits are reported in Table 6 with uncertainties reflecting the variation in fracture width (Table 4). Uncertainties in $\cos\theta$ were ±0.05 based on a random sampling of fracture widths. The parametric fits were done over discrete intervals because the input data, the fracture widths, were also discrete. The fits are superimposed on plots of the data in Figures 8 and 9. The wetting angles calculated for the first uptakes ranged from 63 to 84°. The Cai model did

not work well for calculating wetting angles for the second uptakes as the effective channel size had to be increased to simulate the results, even if the calculated wetting angles for the DI water and sodium chloride solutions were set to zero, indicating completely water-wet surfaces.

■ DISCUSSION

Initial Imbibition. According to eq 8, the primary parameters that affect the rate of imbibition rate between two flat, unreactive parallel plates are the fracture width, the physical properties of the fluid, and the contact angle, which represent interfacial energy. Our experiments showed little difference in imbibition rates for water, sodium bicarbonate, and sodium chloride solutions between fractures oriented parallel and perpendicular to bedding (Figure 6). The physical properties of the fluids (Table 3) varied only slightly, and there was no apparent correlation between these differences and the imbibition data. This lack of variation in imbibition rates suggests that the initial uptake is relatively unaffected by chemical interactions between the fluids and the rock, and that any chemical reactions at the solution/mineral interface are unlikely to alter imbibition rates significantly over the time scale of our observations (2−3 min). The mean widths of the fractures cut parallel to the bedding ranged from 35 to 40 μm, whereas those of the fractures cut perpendicular to the bedding ranged from 41 to 92 μm, ignoring irregularities at the entrance to the fractures. It is possible that the roughness imposed during polishing masked any effects arising from the wetting properties of the fluids. However, the lack of a dependence on concentration agrees with the findings of Sghaier and colleagues.[50] They conducted experiments investigating the effect of sodium chloride concentration on the contact angle between the solution and hydrophobic and hydrophilic surfaces. Their results showed that concentration had a significant effect on glass hydrophilic surfaces, where the contact angle increased from 35 to 45° with concentration. Less hydrophilic surfaces with contact angles up to 90°, such as the shale fractures studied in this experiment, did not show a significant change in the interaction with salt concentrations up to a mass fraction of 26%.

When the imbibition curve is broken into separate segments, the Schwiebert−Leong imbibition model fits the data reasonably well (P-value <0.001). Contact angles derived from this equation and measured fracture widths varied from 51 to 90°, with an averaged dynamic contact angle of 80.1 ± 5.1° (±σ). This is quite similar to values determined by DiStefano and colleagues[3] for water and EF-DI-PR (78°) and EF-DI-PL (71°) and to those determined by Peng and Xiao[51] (82 ± 3°) for water imbibed into the Eagle Ford shale. Correcting for the effect of hydrostatic pressure narrowed the range of calculated wetting angles from 63 to 84°, with an average value of 76 ± 7°.

As suggested by the step-wise imbibition curve described above (Figure 6), averaged sorptivities were not a good description of water uptake, as the rate of uptake changed abruptly as it progressed up the sample. This effect was particularly obvious for data from sample EF-HCO3-PL, which displayed five distinct ranges with different square roots of time dependencies (Figure 6). These oscillations were analyzed using the Schwiebert−Leong approach because the Cai analysis is best applied to monotonically narrowing fractures. The generated dynamic contact angles for regions with the fast and slow flow rates were 62 ± 10° and 84 ± 6°, respectively.
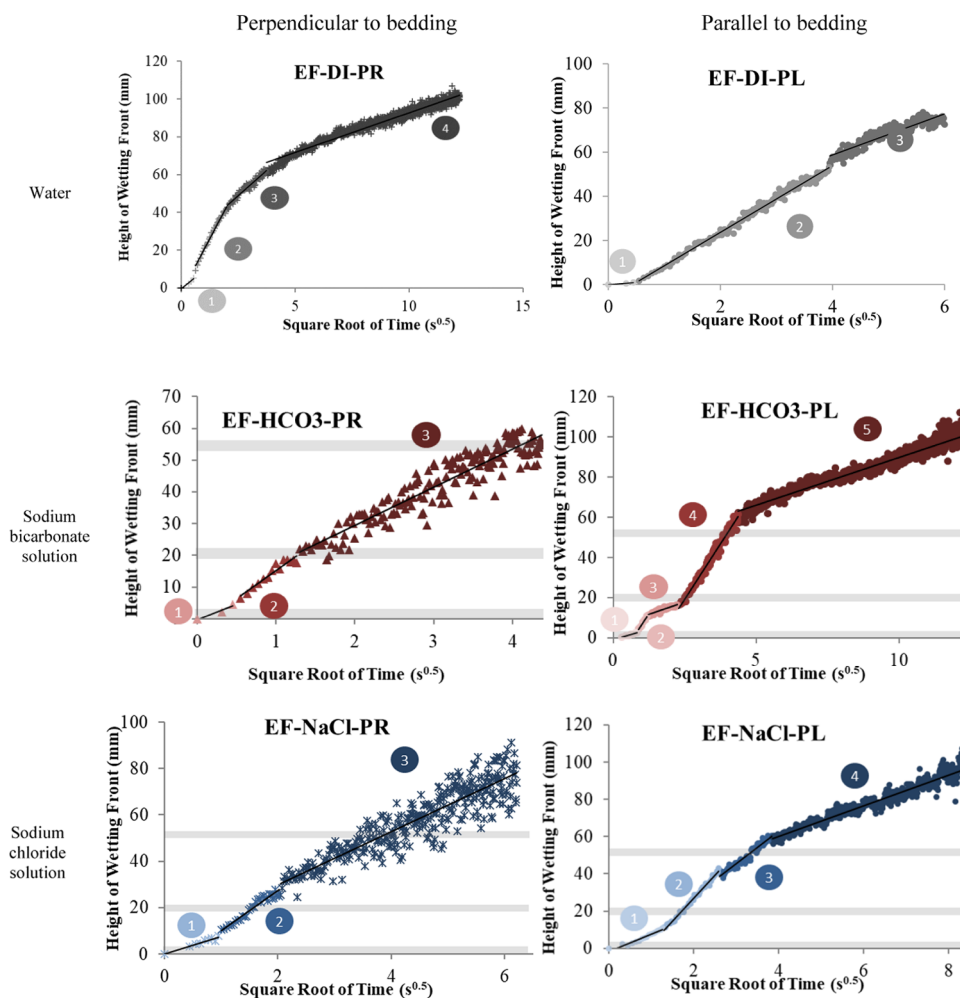
Figure 6. Solution uptake as a function of the square root of time with the model fit. The gray bars indicate where uptake occurred into the part of the fracture that was analyzed for fracture width with X-ray CT. The numbers correspond to the regions given in Table 5. P-values <0.001.

Table 5. Uptake Slopes from Linear Regressions of Data Presented in Figure 6

slope (mm·s$^{-0.5}$)					
time interval (s)					
range (mm)	region 1	region 2	region 3	region 4	region 5
DI ($\perp$)	9.05	22.9	10.7	4.21	
interval	0–0.4	0.5–4.3	4.3–14.2	14.2–149	completely wet
range	0–6	6–51	51–85	85–134	
DI ($\parallel$)	2.03	15.1	9.27	1.54	
interval	0–0.2	0.2–15.4	15.4–35.4	35.4–140	
range	0–1	1–60	60–101	101–110	
NaHCO$_3$ ($\perp$)	6.56	18.2	12.0	no data	
interval	0–0.2	0.2–0.8	0.8–19.1	no data	
range	0–4	4–18	18–70		
NaHCO$_3$ ($\parallel$)	4.14	22.1	4.92	22.0	4.80
interval	0–0.7	0.7–1.4	1.4–5.1	5.1–21.4	21.4–158.9
range	0–3	3–22	22–31	31–120	120–177
NaCl ($\perp$)	7.81	17.1	11.5		
interval	0–0.9	0.9–4.3	4.3–39.2	completely wet	
range	0–7	7–39	39–107		
NaCl ($\parallel$)	9.27	24.7	17.4	8.27	
interval	0–3.2	3.2–6.9	6.9–13.9	13.9–69.9	
range	0–17	17–64	64–119	110–172	

These could be grouped in this manner because the sorptivities of ranges 1, 3, and 5 were similar ($\sim$5 mm·s$^{-0.5}$), as were those of the two alternating ranges (2 and 4, $\sim$22 mm·s$^{-0.5}$). The similarities of these values between the samples indicate that
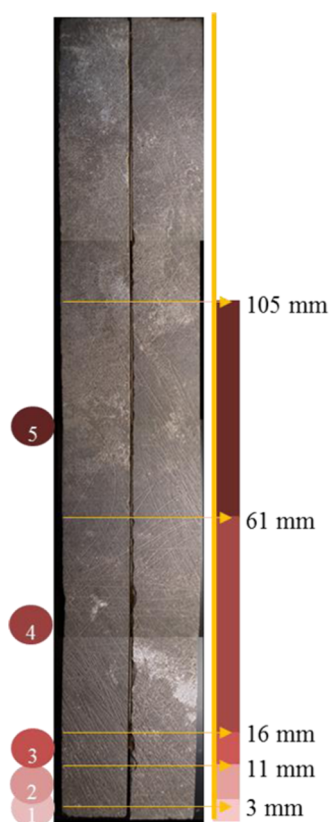
Figure 7. Fracture surface of the EF-HCO3-PL sample. The ranges of uptake identified in Figure 6 and Table 6 are outlined.

Table 6. Uptake Ranges Identified in Samples and Calculated Dynamic Contact Angles Using the Model Developed by Cai et al. (2010)

range	width by X-ray CT (μm)	approximate height up the fracture (mm)	period (s)	contact angles (deg)
		EF-DI-PR uptake 1		
1	130	0−10	0−0.4	81
2	99	10−80	0.9−47	73
3	45	90−110	98−205	78
		EF-DI-PL		
1	51	0−2.3	0−5	82
2	40	2.3−80	5−27	70
		EF-HCO3-PR		
1	56	0−10	0−0.3	70
2	40	15−40	1−9	70
3	34	45−56	13−22	70
		EF-HCO3-PL		
1	60	0−1.5	0−0.009	73
2	55	5−8	0.3−0.9	84
3	41	15−20	3−5	81
4	34	35−55	8−22	74
5	41	65−110	34−144	76
		EF-NaCl-PR		
1	30	0−5	0−0.5	84
2	36	14−90	0.6−31	60
		EF-NaCl-PL		
1	61	0−15	0−2.8	84
2	57	25−40	2.9−8.6	76
3	45	50−100	13−74	73

the ranges of the contact angle are also similar. Such alternating regions of repeated contact angles are typical of convergent−divergent behavior in capillary uptake, as described by Staples and Shaffer and Erickson, Li, and Park, where the flow channel narrows and widens over the length of the sample.[49,52] A hypothesis of constrained flow midway up the fracture is also supported by the X-ray CT evidence of a narrowing midway up the samples.

Another explanation for the observed oscillations is that they arise from variations in dynamic contact angle attributable to mineralogical layers along the shale fracture. In such a case, if the fracture were oriented parallel to the bedding, the fluid would be expected to contact only a single bedding plane with an approximately constant mineralogy. However, examination of EF-HCO3-PL showed that the fracture was, in fact, slightly inclined to the bedding plane, which could have allowed it to cross between calcite-rich to quartz-rich layers. Figure 7 shows the fracture surface of EF-HCO3-PL with the corresponding ranges marked. A similar effect was observed in EF-HCO3-PR, although it was not as pronounced.

However, our results indicate that fluid−mineral interactions did not significantly alter imbibition rates in the shales, at least for the first uptake of DI water and sodium chloride solutions. Unlike more porous systems,[43] in which deviations from square root of time dependence have been reported as arising from the complex porosity of shales,[53] uptake in our experiments appears to be primarily governed by the fracture geometry. However, correlations of measured mineralogy and uptake rates will be needed to better understand the role of such variations in natural fractures. For instance, the presence of calcite may have affected the imbibition of bicarbonate solutions in these experiments as the rates were markedly different. This effect could be explored using X-ray fluorescence along the fracture to test for varying composition and compare it with changes in uptake.

Secondary Imbibition. The results discussed to this point reflect initial values on unwetted surfaces. Wan and colleagues showed that reactions between mineral surfaces and fluids can change contact angles over time.[54] Thus, the effects of contact time were examined by repeating some of the experiments with identical fluids.

To test the effect of repeated exposure of the sample to the fluid, imbibition was repeated after the samples were soaked in DI water and dried to remove accessible residual salts. Figures 8 and 9 show the rates of initial and secondary imbibition for samples with fractures oriented parallel and perpendicular to bedding, respectively. Secondary imbibition rates were much faster than initial rates for the DI and the NaCl fluids, but the sodium bicarbonate experiment (EF-HCO3-PR) showed no change in the imbibition rate. The ratios of the slopes of the primary and secondary imbibitions are 2.0 for EF-DI-PR and EF-DI-PL; 5.1 for EF-NaCl-PR and 2.4 for EF-NaCl-PL; and 0.96 for EF-HCO3-PR. From eq 8, which is valid early in the imbibition process, this indicates a reduction in the dynamic contact angle of 0−6° for rewetting with DI and 4−10° for rewetting with sodium chloride, and no change for the bicarbonate sample. Thus, a "static" contact angle only partially captures the physics of the imbibition process. A more complex thermodynamic/kinetic model is needed that describes the interactions of the brine with mineral surfaces comprised of surface-active organics, such as that described by Awolayo and colleagues.[55]
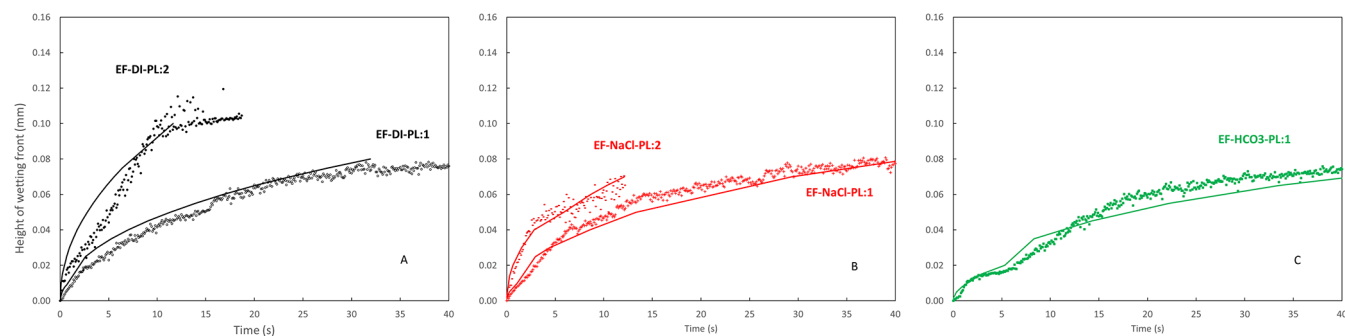
Figure 8. Secondary vs initial imbibition rates of fluids into fractures oriented parallel to the bedding. (A) DI uptakes are in black (first-open circles, second-filled circles), (B) NaCl solution uptakes are in red (first crosses, second dashes), and (C) the first bicarbonate uptake in green (filled squares). The Cai models are shown as solid lines on the plots.
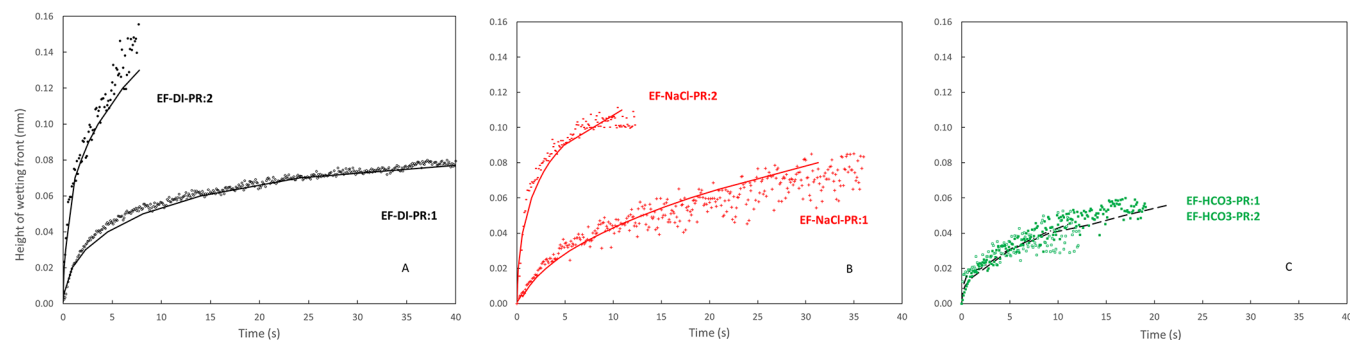

Figure 9. Secondary vs initial imbibition rates of fluids into fractures oriented perpendicular to the bedding. (A) DI uptakes are in black (first-open circles, second-filled circles), (B) NaCl solution uptakes are in red (first crosses, second dashes), and (C) the bicarbonate uptakes are in green (first-open squares, second-filled squares). The Cai models are shown as lines on the plots.

The more rapid rate of the second imbibition relative to the first indicates that the wettability of the fracture surface increased for the DI water and sodium chloride solutions after initial imbibition. This has been observed by Song and colleagues for low-salinity brines.[56] The increase could be due to the hydration of the fracture surface, as suggested by Chenevert, which would lead to increased surface stress via one or more of several mechanisms.[57] Indeed, Chenevert observed that montmorillonite clay swelling occurred in intact clay specimens in the order of minutes to hours. Such alternation would not have affected the initial rise of water in the fracture but could have affected subsequent uptakes because the water was not removed from the fracture immediately after the initial experiment. The samples may also not have been dried thoroughly enough to remove water from clay interlayers. Both chloritic and illitic shales have also demonstrated this behavior, suggesting that the sodium chloride brine would produce a similar effect to DI water.

Other processes may have also affected the time dependence of the uptake rate. These could arise from changes in the interactions between organic components such as asphaltenes and resins upon contact with brines.[58] Such organic molecules assume surfactant-like properties, modifying surface energies, a process that depends on the brine salinity. The bicarbonate solution, which did not exhibit the same behavior as the other fluids, may have been affected by the difference in its pH (8−9) relative to the point of zero charge of the clay (3.4).[59] Alternatively, the dissolution or reaction of the minerals on the fracture surface can increase the fracture roughness, increasing the wettability of hydrophilic surfaces for contact angles <90°.[12] Any residual adsorbed water remaining from the first

imbibition would also be expected to have affected the second uptake.[60]

Unlike the DI and NaCl experiments, the secondary imbibition rate was the same as the initial imbibition rate in the sodium bicarbonate sample. This implies that no changes in the wettability occurred between the two uptakes, reflecting the complexity of surface interactions that depend on pH and salinity. The surface charge of shale minerals will depend on pH and can switch from being water wet to oil wet and back again, depending on salinity.[61] The shale samples studied here are calcite-rich, suggesting that the surface will become charged.[62,63] The initial contact with the bicarbonate solution may have created a stable mineral−brine interface, preventing the sample from experiencing degradation from hydration and preserving a less hydrophilic fracture surface.[64]

Application to Oil−Brine−Rock Interactions. In these experiments, we were mainly interested in the rate of transport of the fluid through the reservoir and whether-or-not it could be described by capillary flow models. Displacement of a hydrocarbon-saturated phase would be an interesting extension to the work and build on shale porosity studies done earlier by our group.[65,66] In these previous studies, we found that much of the hydrocarbon content was trapped in very small-pore volumes and extraction of these materials was through connected nanoscale connected porosities.

■ CONCLUSIONS

Shale formations are increasingly important as sources for shale oil/gas and as potential reservoirs or reservoir seals for geological carbon sequestration. Models of fluid flow are used

to predict extraction efficiency, storage capacity, and long-term stability of shale reservoirs, but these models require well-defined rock−fluid interaction parameters. This study measured fracture imbibition rates in Eagle Ford shale samples using neutron radiography to better understand the imbibition process during fluid flow and to determine dynamic contact angles during imbibition.

Imbibition rates were measured by determining the height of the wetting front over time. Sodium bicarbonate and sodium chloride solutions were chosen to reflect important components of subsurface reservoir fluids and were compared with pure water, which was analyzed in a previous study. Imbibition into fractures oriented parallel and perpendicular to the bedding were imaged to determine the effects of the bedding, and a multipart sorptivity model was fit to the data to estimated contact angles.

Generally, the results of the first imbibition for different fluids were strikingly similar. The systems were slightly water wet to start, with contact angles trending toward 90°. With corrections for hydraulic pressure, the imbibition data was fit to an average contact angle of 76 ± 7°, within the range reported in earlier investigations.[3] However, for most samples, particularly the bicarbonate-contacted uptake in EF-HCO3-PL, a single contact angle did not describe the behavior in sufficient detail. The uptake rate was sectional, and contact angles were found to vary between 62 ± 10° and ∼84 ± 6° as the fluid rose, likely reflecting a longitudinal narrowing and widening of the fracture.

A second exposure of the samples to the identical fluid showed that secondary imbibition rates were quicker than primary imbibition rates for samples exposed to DI or to sodium chloride solution. This indicated that initial contact with DI or sodium chloride solutions had altered the fracture surface, which suggests that imbibition rates in shale formations may increase with successive fracturing and/or longer-term fluid exposure. The same effect was not observed for sodium bicarbonate uptakes, suggesting that the bicarbonate ion prevented the hydration of shale minerals. This may reflect the pH of the solution relative to the points of zero charge of the minerals involved, especially the carbonates.

Within the range of compositions examined, our results showed that fluid uptake depends on both the fracture structure and the height of the wetting front. The effects of aqueous solution chemistry on imbibition rate appear to be relatively minor initially but cause a significant increase in the uptake rate with longer exposure. Analysis of our data showed that a simple model of capillary flow can be used to determine contact angles for various solutions in contact with the shale or other materials. However, its application requires analysis of the fracture on a relatively fine scale. Thus, these variations in time and space necessitate a more complex description of wetting for reservoir modeling.

■ MATERIALS AND METHODS

Sample Preparation for Imbibition Measurements. Six samples of synthetic fractures created from paired shale blocks were prepared for analysis. Before assembly, the fracture surface on each block was polished with a 180 grit lapping plate until no light was observed to pass through the fracture when the blocks were held together. The samples were rinsed (after polishing) and dried to a constant mass before the blocks were clamped together and the seam sealed with Kapton tape (DuPont, Wilmington, Delaware) to create a nearly planar

synthetic fracture with openings ranging from <3.68 to ∼500 μm. Kapton tape was ideal for fastening the shale blocks together for this application because it is only 25 μm thick and only minimally attenuates neutrons.

Solution Preparation. Two solutions, one of sodium bicarbonate and one of sodium chloride, were prepared for imbibition experiments. The sodium bicarbonate solution was made by dissolving 46 g of sodium bicarbonate in 500 mL of DI water (18 MΩ·cm, degassed by sparging with argon for 0.5 h), resulting in a 1.1 mol·L^{-1} solution. The sodium chloride solution was made by dissolving 18 g of sodium chloride into 500 mL of DI water, yielding a 0.6 mol·L^{-1} sodium chloride solution. Both were stirred overnight at room temperature to dissolve the solute.

Nondestructive Fracture Characterization. The sample fracture widths were characterized using X-ray computed tomography (CT) scans performed at Argonne National Laboratory's Advanced Photon Source using the GSECARS tomography beamline (13-BM-D). Fifty-five kiloelectron volt X-rays were used to image the samples with the fracture plane oriented perpendicular to the CT slice plane. Each scan comprised 900 angular projections from 0 to 360°. The final images had a voxel edge length of 3.68 μm. Three scans were taken on each core, which each captured a 7 mm wide subvolume centered around the fracture with a 12.7 mm depth, d. Each scan captured a 3 mm long segment of the fracture: one covering the bottom 0−3 mm of the fracture, one 18−21 mm from the bottom, and one 50−53 mm from the bottom. The bottom of the fracture was set as the surface initially in contact with the imbibing fluid.

The fracture widths in each X-ray CT stack were analyzed by first segmenting the images in ImageJ[67] via the Trainable Weka Segmentation macro,[68] which allowed the fracture to be differentiated from the rock. The CT images were then loaded into the Dragonfly 3D visualization and image analysis software (Object Research Systems Inc., Montreal, Canada) to determine the fracture thickness by calculating the diameter of a hypothetical sphere that could fit within the fracture boundary. The 3D fracture thickness was displayed using color coding corresponding to the scaler values of the fracture thickness.

Spontaneous Imbibition Measured with Neutron Imaging. Spontaneous imbibition was measured for all samples at the BT-2 neutron imaging facility at the National Institute of Standards and Technology Center for Neutron Research. The imbibition experiments were performed in the same manner as those described earlier.[3,43] The fractured samples were oriented, so the neutron beam passed the vertical plane of the fracture. An aluminum pan of fluid, either sodium bicarbonate or sodium chloride, was then raised using a remote-controlled vertical stage until the imbibing fluid just touched the bottom of the sample. Image collection was begun before the fluid contacted the rock sample, and images were collected every 0.1 s during the experiment as the fluid was imbibed into the fracture. The images had pixel edge lengths of 55 μm. The large contrast in neutron images between the empty fracture and the fluid allowed the fluid movement to be visualized with time.

Before analyzing a set of images, all pixels in all images in the set were normalized according to eq 10 to form the transmission image, T_i.

$$T_i = \frac{I_S - I_{DF}}{I_R - I_{DF}} \qquad (10)$$

where I_S is the measured image intensity of each pixel, I_{DF} is the dark field intensity of that pixel obtained with the shutter closed, and I_R is the intensity of that pixel in a reference image. The reference was an image of the rock/fracture system taken immediately before imbibition commenced. Normalizing the experimental images to the reference allowed any contributions from the rock to be removed, producing a time-resolved sequence of fluid imbibition images with a frame rate of 10 images per second. Approximately, 180−1500 frames were obtained during each experiment, which was run until the fracture was completely full; run times ranged from about 0.3 to 2.5 min.

Certain trade names and company products are mentioned in the text or identified in figures to adequately specify the experimental procedure and equipment used. This identification does not imply recommendation or endorsement by the National Institute of Standards and Technology and Oak Ridge National Laboratory, nor does it imply that the products are necessarily the best available for the purpose.

■ AUTHOR INFORMATION

Corresponding Author

Joanna McFarlane − *Oak Ridge National Laboratory, Oak Ridge, Tennessee 37831, United States;* ⊙ orcid.org/0000-0002-4112-5104; Email: mcfarlanej@ornl.gov

Authors

Victoria H. DiStefano − *Oak Ridge National Laboratory, Oak Ridge, Tennessee 37831, United States; Bredesen Center, University of Tennessee, Knoxville, Tennessee 37996-3394, United States; U.S. Department of Energy, Germantown, Maryland 20874, United States*

Philip R. Bingham − *Oak Ridge National Laboratory, Oak Ridge, Tennessee 37831, United States*

Hassina Z. Bilheux − *Oak Ridge National Laboratory, Oak Ridge, Tennessee 37831, United States*

Michael C. Cheshire − *Oak Ridge National Laboratory, Oak Ridge, Tennessee 37831, United States; Chevron, The Woodlands, Texas 77830, United States*

Richard E. Hale − *Oak Ridge National Laboratory, Oak Ridge, Tennessee 37831, United States*

Daniel S. Hussey − *Physical Measurements Laboratory, National Institute of Standards and Technology, Gaithersburg, Maryland 20899, United States;* ⊙ orcid.org/0000-0002-2851-4367

David L. Jacobson − *Physical Measurements Laboratory, National Institute of Standards and Technology, Gaithersburg, Maryland 20899, United States*

Lindsay Kolbus − *Oak Ridge National Laboratory, Oak Ridge, Tennessee 37831, United States; Indianapolis Metropolitan High School, Indianapolis, Indiana 46222, United States*

Jacob M. LaManna − *Physical Measurements Laboratory, National Institute of Standards and Technology, Gaithersburg, Maryland 20899, United States*

Edmund Perfect − *Department of Earth and Planetary Science, University of Tennessee, Knoxville, Tennessee 37996-1526, United States*

Mark Rivers − *University of Chicago, Geophysical Sciences, Argonne, Illinois 60439, United States;* ⊙ orcid.org/0000-0003-4728-4189

Louis J. Santodonato − *Oak Ridge National Laboratory, Oak Ridge, Tennessee 37831, United States; Advanced Research Systems, Macungie, Pennsylvania 18062, United States*

Lawrence M. Anovitz − *Oak Ridge National Laboratory, Oak Ridge, Tennessee 37831, United States;* ⊙ orcid.org/0000-0002-2609-8750

Complete contact information is available at:
https://pubs.acs.org/10.1021/acsomega.1c04177

Notes

The authors declare no competing financial interest.

■ ACKNOWLEDGMENTS

■ REFERENCES

(1) Anovitz, L. M.; Cole, D. R. Analysis of the Pore Structures of Shale Using Neutron and X-Ray Small Angle Scattering. In *Geological Carbon Storage: Subsurface Seals and Caprock Integrity*; John Wiley & Sons, 2019; pp 71−118.

(2) Fisher, K.; Warpinski, N. R. Hydraulic-fracture-height growth: Real data. *SPE Prod. Oper.* **2012**, *27*, 8−19.

(3) DiStefano, V. H.; Cheshire, M. C.; McFarlane, J.; Kolbus, L. M.; Hale, R. E.; Perfect, E.; Bilheux, H. Z.; Santodonato, L. J.; Hussey, D. S.; Jacobson, D. L.; LaManna, J. M.; Bingham, P. R.; Starchenko, V.; Anovitz, L. M. Spontaneous imbibition of water and determination of effective contact angles in the Eagle Ford Shale Formation using neutron imaging. *J. Earth Sci.* **2017**, *28*, 874−887.

(4) Abdallah, W.; Buckley, J.; Carnegie, A.; Edwards, J.; Herold, B.; Fordham, E.; Graue, A.; Habashy, T.; Seleznev, N.; Signer, C.; Hussain, H.; Montaron, B.; Ziauddin, M. Fundamentals of Wettability. *Oilfield Rev.* **2007**, *19*, 44−61.

(5) Anderson, W. G. Wettability Literature Survey-Part 1: Rock.Oil/Brine lnteractions and the Effects of Core Handling on Wettability. *J. Pet. Technol.* **1986**, *38*, 1125−1144.

(6) Anderson, W. G. Wettability Literature Survey-Part 2: Wettability Measurement. *J. Pet. Technol.* **1986**, *38*, 1246−1262.

(7) Anderson, W. G. Wettability Literature Survey-Part 3: The Effects of Wettability on the Electrical Properties of Porous Media. *J. Pet. Technol.* **1986**, *38*, 1371−1378.

(8) Anderson, W. O. *Wettability Literature Survey-Part 4: The Effects of Wettability on Capillary Pressure*; Society of Petroleum Engineering: Richardson, TX, 1986; SPE 15271.

(9) Zhang, Y.; Taboada-Serrano, P. Model for gas-hydrate equilibrium in porous media that incorporates pore-wall properties. *Phys. Chem. Chem. Phys.* **2020**, *22*, 10900.

(10) Young, T. An essay on the cohesion of fluids. *Philos. Trans. R. Soc. London* **1805**, *95*, 65−87.

(11) Gao, Z.; Hu, Q. Wettability of Mississippian Barnett Shale samples at different depths: Investigations from directional spontaneous imbibition. *AAPG Bull.* **2016**, *100*, 101−114.

(12) Wenzel, R. N. Resistance of solid surfaces to wetting by water. *Ind. Eng. Chem.* **1936**, *28*, 988−994.

(13) Hamraoui, A.; Thuresson, K.; Nylander, T.; Yaminsky, V. Can a dynamic contact angle be understood in terms of a friction coefficient? *J. Colloid Interface Sci.* **2000**, *226*, 199−204.

(14) Chen, C.; Wan, J.; Li, W.; Song, Y. Water contact angles on quartz surfaces under supercritical CO_2 sequestration conditions: Experimental and molecular dynamics simulation studies. *Int. J. Greenhouse Gas Control* **2015**, *42*, 655−665.

(15) Zhou, Q.; Birkholzer, J. T.; Tsang, C.-F.; Rutqvist, J. A method for quick assessment of CO_2 storage capacity in closed and semi-closed saline formations. *Int. J. Greenhouse Gas Control* **2008**, *2*, 626−629.

(16) US Geologic Survey Carbon Dioxide Storage Resources Assessment Team, *National Assessment of Geologic Carbon Dioxide Storage Resources − Results*, USGS Circular 1386, Version 1.1, September 2013.

(17) Glenn, E. P.; Brown, J. J.; Leary, J. W. Irrigating Crops with Seawater. *Sci. Am.* **1998**, *279*, 76−81.

(18) Cheng, C.; Perfect, E.; Donnelly, B.; Bilheux, H.; Tremsin, A.; McKay, L.; DiStefano, V.; Cai, J.; Santodonato, L. Rapid imbibition of water in fractures within unsaturated sedimentary rock. *Adv. Water Resour.* **2015**, *77*, 82−89.

(19) Perfect, E.; Cheng, C.; Kang, M.; Bilheux, H.; Lamanna, J.; Gragg, M.; Wright, D. Neutron imaging of hydrogen-rich fluids in geomaterials and engineered porous media: A review. *Earth-Sci. Rev.* **2014**, *129*, 120−135.

(20) Kang, M.; Perfect, E.; Cheng, C. L.; Bilheux, H. Z.; Gragg, M.; Wright, D. M.; Lamanna, J. M.; Horita, J.; Warren, J. M. Diffusivity and sorptivity of Berea sandstone determined using neutron radiography. *Vadose Zone J.* **2013**, *12*, No. vzj2012.0135.

(21) Hassanein, R.; Meyer, H.; Carminati, A.; Estermann, M.; Lehmann, E.; Vontobel, P. Investigation of water imbibition in porous stone by thermal neutron radiography. *J. Phys. D: Appl. Phys.* **2006**, *39*, 4284.

(22) Middleton, M.; Li, K.; de Beer, F. In *Spontaneous Imbibition Studies of Australian Reservoir Rocks with Neutron Radiography*, SPE Western Regional Meeting; Society of Petroleum Engineers, 2005; SPE-93634.

(23) Swinehart, D. The Beer-Lambert law. *J. Chem. Educ.* **1962**, *39*, No. 333.

(24) Kardjilov, N.; Dawson, M.; Hilger, A.; Manke, I.; Strobl, M.; Penumadu, D.; Kim, F. H.; Garcia-Moreno, F.; Banhart, J. A highly adaptive detector system for high resolution neutron imaging. *Nucl. Instrum. Methods Phys. Res., Sect. A* **2011**, *651*, 95−99.

(25) Hussey, D. S.; LaManna, J. M.; Baltic, E.; Jacobson, D. L. Neutron imaging detector with 2 μm spatial resolution based on event reconstruction of neutron capture in gadolinium oxysulfide scintillators. *Nucl. Instrum. Methods Phys. Res., Sect. A* **2017**, *866*, 9−12.

(26) Hilger, A.; Kardjilov, N.; Kandemir, T.; Manke, I.; Banhart, J.; Penumadu, D.; Manescu, A.; Strobl, M. Revealing microstructural

inhomogeneities with dark-field neutron imaging. *J. Appl. Phys.* **2010**, *107*, No. 036101.

(27) LaManna, J.; Hussey, D. S.; Baltic, E.; Jacobson, D. L. In *Composition Determination of Shale with Simultaneous Neutron and X-ray Tomography*, American Geophysical Union Fall Meeting, New Orleans, December 11−15, 2017.

(28) Zhang, S.; Li, Y.; Pu, H. Studies of the storage and transport of water and oil in organic-rich shale using vacuum imbibition method. *Fuel* **2020**, No. 117096.

(29) Peng, Y. Analytical, Computational and Experimental Studies of Capillary Flow in Complex Geometries. Ph.D. Dissertation, Western Michigan Univeristy, 2009.

(30) Liu, H.; Cao, G. Effectiveness of the Young-Laplace equation at nanoscale. *Sci. Rep.* **2016**, No. 23936.

(31) Washburn, E. W. The dynamics of capillary flow. *Phys. Rev.* **1921**, *17*, 273.

(32) Lucas, R. Rate of capillary ascension of liquids. *Kolloid-Z.* **1918**, *23*, 15−22.

(33) Fisher, L. R.; Lark, P. D. An experimental study of the Washburn equation for liquid flow in very fine capillaries. *J. Colloid Interface Sci.* **1979**, *69*, 486−492.

(34) Dong, M.; Chatzis, I. The imbibition and flow of a wetting liquid along the corners of a square capillary tube. *J. Colloid Interface Sci.* **1995**, *172*, 278−288.

(35) Schwiebert, M. K.; Leong, W. H. Underfill flow as viscous flow between parallel plates driven by capillary action. *IEEE Trans. Compon., Packag., Manuf. Technol., Part C* **1996**, *19*, 133−137.

(36) Han, A.; Mondin, G.; Hegelbach, N. G.; de Rooij, N. F.; Staufer, U. Filling kinetics of liquids in nanochannels as narrow as 27 nm by capillary force. *J. Colloid Interface Sci.* **2006**, *293*, 151−157.

(37) Berthier, J.; Gosselin, D.; Berthier, E. A generalization of the Lucas−Washburn−Rideal law to composite microchannels of arbitrary cross section. *Microfluid. Nanofluid.* **2015**, *19*, 497−507.

(38) Cai, J.-C.; Yu, B.-M.; Mei, M.-F.; Luo, L. Capillary rise in a single tortuous capillary. *Chin. Phys. Lett.* **2010**, *27*, No. 054701.

(39) Rietveld, H. A profile refinement method for nuclear and magnetic structures. *J. Appl. Crystallogr.* **1969**, *2*, 65−71.

(40) Chermak, J. A.; Schreiber, M. E. (2014). Mineralogy and trace element geochemistry of gas shales in the United States: Environmental implications. *Int. J. Coal Geol.* **2014**, *126*, 32−44.

(41) Engle, M. A.; Doolan, C. A.; Pitman, J. A.; Varonka, M. S.; Chenault, J.; Orem, W. H.; McMahon, P. B.; Jubb, A. M. Origin and geochemistry of formation waters from the lower Eagle Ford Group, Gulf Coast Basin, south central Texas. *Chem. Geol.* **2020**, *550*, No. 119754.

(42) Blondes, M. S.; Gans, K. D.; Engle, M. A.; Kharaka, Y. K.; Reidy, M. E.; Saraswathula, V.; Thordsen, J. J.; Rowan, E. L.; Morrissey, E. A. *U.S. Geological Survey National Produced Waters Geochemical Database* (ver. 2.3, January 2018); U.S. Geological Survey Data Release, 2018.

(43) Horodecky, B. B.; Perfect, E.; Bilheux, H. Z.; Brabazon, J. W.; Gates, C. H. Onset dynamics of air-water menisci on rock fracture surfaces. *Adv. Water Resour.* **2020**, *146*, No. 103754.

(44) Ozdemir, O.; Karakashev, S. I.; Nguyen, A. V.; Miller, J. D. Adsorption of carbonate and bicarbonate salts at the air−brine interface. *Int. J. Miner. Process.* **2006**, *81*, 149−158.

(45) Ozdemir, O.; Celik, M.; Nickolov, Z.; Miller, J. Water structure and its influence on the flotation of carbonate and bicarbonate salts. *J. Colloid Interface Sci.* **2007**, *314*, 545−551.

(46) Haynes, W. M. *CRC Handbook of Chemistry and Physics*; CRC Press, 2012.

(47) Ozbek, H.; Fair, J.; Phillips, S. *Viscosity of Aqueous Sodium Chloride Solutions from 0-150 °C*; Ernest Orlando Lawrence Berkeley National Laboratory: Berkeley, CA, 1977; LBL-5391.

(48) Chen, H.; Li, Z.; Wang, F.; Wang, Z.; Li, H. Investigation of surface properties for electrolyte solutions: Measurement and prediction of surface tension for aqueous concentrated electrolyte solutions. *J. Chem. Eng. Data* **2017**, *62*, 3783−3792.

(49) Staples, T. L.; Shaffer, D. G. Wicking flow in irregular capillaries. *Colloids Surf., A* **2002**, *204*, 239−250.

(50) Sghaier, N.; Prat, M.; Nasrallah, S. B. On the influence of sodium chloride concentration on equilibrium contact angle. *Chem. Eng. J.* **2006**, *122*, 47−53.

(51) Peng, S.; Xiao, X. Investigation of multiphase fluid imbibition in shale through synchrotron-based dynamic micro-CT imaging. *J. Geophys. Res.: Solid Earth* **2017**, *122*, 4475−4491.

(52) Erickson, D.; Li, D.; Park, C. B. Numerical simulations of capillary-driven flows in nonuniform cross-sectional capillaries. *J. Colloid Interface Sci.* **2002**, *250*, 422−430.

(53) Roychaudhuri, B.; Tsotsis, T. T.; Jessen, K. An experimental investigation of spontaneous imbibition in gas shales. *J. Pet. Sci. Eng.* **2013**, *111*, 87−97.

(54) Wan, J.; Kim, Y.; Tokunaga, T. K. Contact angle measurement ambiguity in supercritical CO_2−water−mineral systems: Mica as an example. *Int. J. Greenhouse Gas Control* **2014**, *31*, 128−137.

(55) Awolayo, A. N.; Sarma, H. K.; Nghiem, L. X. Modeling the characteristic thermodynamic interplay between potential determining ions during brine-dependnt recovery process in carbonate rocks. *Fuel* **2018**, *224*, 701−717.

(56) Song, J.; Wang, Q.; Shaik, I.; Puerto, M.; Bikkina, P.; Aichele, C.; Biswal, S. L.; Hirasaki, G. J. Effect of salinity, Mg^{2+} and SO_4^{2-} on "smart water"-induced carbonate wettability alteration in a model oil system. *J. Colloid Interface Sci.* **2020**, *563*, 145−155.

(57) Chenevert, M. E. Shale alteration by water adsorption. *J. Pet. Technol.* **1970**, *22*, 1141−1148.

(58) Honarvar, B.; Rahimi, A.; Safari, M.; Shajehahmadi, S.; Karimi, M. Smart water effects on a crude oil-brine-carbonate rock (CBR) system: Further suggestions on mechanisms and conditions. *J. Mol. Liq.* **2020**, *299*, No. 112173.

(59) Ijagbemi, C. O.; Baek, M.-H.; Kim, D.-S. Montmorillonite surface properties and sorption characteristics for heavy metal removal from aqueous solutions. *J. Hazard. Mater.* **2009**, *166*, 538−546.

(60) Gao, Z.; Hu, Q. Initial water saturation and imbibition fluid affect spontaneous imbibition into Barnett shale samples. *J. Nat. Gas Sci. Eng.* **2016**, *34*, 541−551.

(61) Xie, L.; Lu, S.; Li, J.; Hu, Y.; Zhang, P.; Chen, J.; Zhang, P. Experimental investigations of the mineral wettability in shale and its influence factors. *Acta Geol. Sin.* **2015**, *89*, 170−171.

(62) Collini, H.; Li, S.; Jackson, M. D.; Agenet, N.; Rashid, B.; Couves, J. Zeta potential in intact carbonates at reservoir conditions and its impact on oil recovery during controlled salinity waterflooding. *Fuel* **2020**, No. 116927.

(63) Al Mahrouqi, D.; Vinogradov, J.; Jackson, M. D. Zeta potential of artificial and natural calcite in aqueous solution. *Adv. Colloid Interface Sci.* **2017**, *240*, 60−76.

(64) Haagh, M. E. J.; Schilderink, N.; Mugele, F.; Duits, M. H. G. Wetting of mineral surfaces by fatty-acid-laden oil and brine: Carbonate effect at elevated temperatures. *Energy Fuels* **2019**, *33*, 9446−9456.

(65) DiStefano, V. H.; McFarlane, J.; Stack, A. G.; Perfect, E.; Mildner, D. F. R.; Blueuel, M.; Chipera, S. J.; Littrell, K. C.; Cheshire, M. C.; Manz, K. E.; Anovitz, L. M. Solvent-pore interactions in the Eagle Ford Formation. *Fuel* **2019**, *238*, 298−311.

(66) DiStefano, V. H.; McFarlane, J.; Anovitz, L. M.; Gordon, A. D.; Hale, R. E.; Hunt, R. D.; Lewis, S. A.; Littrell, K. C.; Stack, A. G.; Chipera, S. J.; Perfect, E. Extraction of organic compounds from representative shales and the effect on porosity. *J. Nat. Gas Sci. Eng.* **2016**, *35*, 646−660.

(67) Schneider, C. A.; Rasband, W. S.; Eliceiri, K. W. NIH Image to ImageJ: 25 years of image analysis. *Nat. Methods* **2012**, *9*, 671.

(68) Arganda-Carreras, I.; Kaynig, V.; Rueden, C.; Eliceiri, K. W.; Schindelin, J.; Cardona, A.; Sebastian Seung, H. Trainable Weka Segmentation: a machine learning tool for microscopy pixel classification. *Bioinformatics* **2017**, *33*, 2424−2426.